PHYSICAL REVIEW C **68**, 064602 (2003)

Systematic study of $L\leqslant 3$ giant resonances in Sm isotopes via multipole decomposition analysis

M. Itoh,[1,*] H. Sakaguchi,[1] M. Uchida,[1] T. Ishikawa,[1,†] T. Kawabata,[1,‡] T. Murakami,[1] H. Takeda,[1] T. Taki,[1] S. Terashima,[1]
N. Tsukahara,[1] Y. Yasuda,[1] M. Yosoi,[1] U. Garg,[2] M. Hedden,[2] B. Kharraja,[2] M. Koss,[2] B. K. Nayak,[2] S. Zhu,[2]
H. Fujimura,[3] M. Fujiwara,[3,4] K. Hara,[3] H. P. Yoshida,[3] H. Akimune,[5] M. N. Harakeh,[6] and M. Volkerts[6]
[1]*Department of Physics, Kyoto University, Kyoto 606-8502, Japan*
[2]*Physics Department, University of Notre Dame, Notre Dame, Indiana 46556, USA*
[3]*Research Center for Nuclear Physics (RCNP), Osaka University, Osaka 567-0047, Japan*
[4]*Advanced Science Research Center, Japan Atomic Energy Research Institute, Tokai, Ibaraki 319-1995, Japan*
[5]*Department of Physics, Konan University, Hyogo 658-8501, Japan*
[6]*Kernfysisch Versneller Instituut (KVI), NL 9747 AA Groningen, The Netherlands*
(Received 28 April 2003; published 4 December 2003)

Background-free inelastic scattering spectra have been obtained for five Sm isotopes with 386-MeV α particles at forward angles (including 0°) to investigate the effect of deformation on the compressional-mode giant resonances. The strength distributions for the $L\leqslant 3$ isoscalar giant resonances have been extracted via a multipole decomposition analysis using angular distributions calculated in the framework of the density-dependent single-folding model. We observed a splitting of the giant monopole resonance because of its mixing with the giant quadrupole resonance. For the isoscalar giant dipole resonance, the observed effects of deformation are different for the low- and high-excitation-energy components. Evidence has been obtained for the theoretically predicted mixing between the isoscalar giant dipole resonance and the high energy octupole resonance.

DOI: 10.1103/PhysRevC.68.064602 PACS number(s): 24.30.Cz, 25.55.Ci, 27.60.+j, 27.70.+q

I. INTRODUCTION

The states of collective motion are a common feature of many-body systems. Since such collective states are embedded in the continuum, they are observed as resonances corresponding to transitions between the ground state and the collective states. Among these, the giant monopole resonance (GMR) and the isoscalar giant dipole resonance (ISGDR), which are called the compressional-mode giant resonances, are of considerable interest since their excitation energies directly relate to the incompressibility of nuclear matter, an important component of the nuclear equation of state which plays a crucial role in describing nucleon motion in nuclei, and in cosmological events such as type-II supernova explosions.

It was reported two decades ago that the giant resonance "bump" in the deformed nucleus ^{154}Sm had a larger "lower" component when compared with that in the spherical nucleus ^{144}Sm [1]. This was interpreted as resulting from K splitting of the giant quadrupole resonance (GQR) and a coupling between the GMR and the $K=0$ component of GQR [1,2]. Further evidence for splitting of the isoscalar giant resonances was provided by inelastic electron scattering [3], inelastic ^{3}He scattering [4], and fission decay of ^{238}U induced by inelastic α scattering, i.e., $^{238}\mathrm{U}(\alpha,\alpha' f)$ reaction [5]. However, due to a large amount of instrumental background in all early singles measurements, the peak-to-background ratios were low, and none of these investigations could clearly separate between the GMR and GQR strengths, leading to difficulties in reaching a definitive conclusion. In the $^{238}\mathrm{U}(\alpha,\alpha' f)$ reaction [5], where inelastically scattered α particles were detected at and near 0° in coincidence with fission fragments, the splitting of the monopole resonance was indicated free of any background.

Recently, Youngblood *et al.* [6] have extracted the GMR and GQR strength distributions in ^{154}Sm by fitting the experimental angular distributions with calculated angular distributions of various multipole components. They provided evidence for a mixing between the GMR and the GQR by fitting the observed strength distributions with three Gaussian peaks corresponding to the number of components predicted in the adiabatic cranking model [7]. Their results showed a fair agreement with the calculations of Abgrall *et al.*, but not with several other calculations [8–10].

There have been a few studies dealing with the effect of deformation on the ISGDR and the high energy octupole resonance (HEOR). Theoretically, Nishizaki and Andō predicted the K splitting and the coupling between the ISGDR and HEOR some time ago [11]. Experimentally, Youngblood *et al.* have reported that the ISGDR strength in ^{154}Sm is distributed roughly uniformly [12], and no discernible effect of deformation is observed on the ISGDR strength distribution. In the case of the HEOR, Morsch *et al.*, in measurements on deformed rare-earth and actinide nuclei [13], found a broadening and a shift in the excitation energies of the resonances. However, they could not separate the HEOR from the ISGDR which is also located in the same excitation-energy region.

---

[*] Present address: Research Center for Nuclear Physics, Osaka University, Ibaraki, Osaka 567-0047, Japan.

[†] Present address: Laboratory of Nuclear Science, Tohoku University, Sendai, Miyagi 982-0216, Japan.

[‡] Present address: Center for Nuclear Study, University of Tokyo, Wako, Saitama 351-0198, Japan.

In an earlier paper [14], we reported the results on ^{144}Sm and ^{154}Sm. In this paper, we report the results of a systematic study of both compressional modes of excitation, the GMR and the ISGDR, for the isotopes ^{144,148,150,152,154}Sm, which show gradual change in deformation from the spherical nucleus ^{144}Sm to the deformed nucleus ^{154}Sm. This is the first time that the effect of deformation on the ISGDR has been investigated systematically.

II. EXPERIMENT

The experiments were performed at the Ring Cyclotron Facility of the Research Center for Nuclear Physics (RCNP), Osaka University. ^{4}He^{++} beams were accelerated by the AVF cyclotron and the ring cyclotron up to 386 MeV. At this energy, the contributions from the pickup/breakup processes such as $(\alpha, {}^5\mathrm{He}^*) \rightarrow ({}^5\mathrm{He}^*, \alpha' n)$ and $(\alpha, {}^5\mathrm{Li}^*) \rightarrow ({}^5\mathrm{Li}^*, \alpha' p)$ reactions are expected to be located well beyond the giant resonance region. In order to get clean energy spectra, special care was taken to obtain a high-quality beam. To minimize beam halo, the beam was transported onto the target without any slits following a single-turn extraction from the ring cyclotron. The beam current was 1–20 nA, which was limited by the data-acquisition rate or by the maximum available current of the accelerator. The energy resolution was less than 200 keV, sufficient to investigate the giant resonances of interest which have widths of $\sim$5 MeV.

The halo-free beam bombarded thin (2–10 mg/cm^2), self-supporting, metallic targets of ^{144}Sm, ^{148}Sm, ^{150}Sm, ^{152}Sm, and ^{154}Sm. Inelastically scattered particles were analyzed by the high-resolution magnetic spectrometer Grand Raiden [15]. The vertical and horizontal positions of the α particle in the focal plane were measured with a focal-plane detector system consisting of two multiwire drift chambers (MWDC's) and two plastic scintillation counters (PS1, PS2). The scintillation counters were used to generate trigger signals and to identify α particles via energy-loss signals. Ray-tracing technique was used to reconstruct the horizontal scattering angle. The actual angular resolution of the MWDC's, including the broadening of scattering angle due to the emittance of the ^{4}He^{2+} beam and the multiple Coulomb-scattering effect, was about 0.07°. The vertical acceptance was limited to ±20 mr by a 2-mm-thick tantalum collimator.

The angular distributions were measured with three different settings of the spectrometer system. In the first setting (for the 0° measurement), the primary beam, after passing through the spectrometer, was guided to a beam pipe located at the high momentum side of the focal-plane detector and was stopped in a Faraday cup (FC) placed several meters downstream from the detectors. The last dipole magnet was used as a steering magnet with a bending angle of 1°–2° to collect all electric charges of α beams in the 0° FC. The schematic layout of the setup for the 0° measurement is shown in Figs. 1(a) and 1(b). In order to reduce background events due to secondary scattered electrons from PS1, a 1.5-mm-thick aluminum board was placed between PS1 and PS2. The scattered α particles passing through the nonsensitive areas of MWDC's were stopped at a lead block placed near the beam pipe between MWDC1 and MWDC2. The trigger rate with an empty target frame was lower than 5 cps for a beam current of 1 nA.

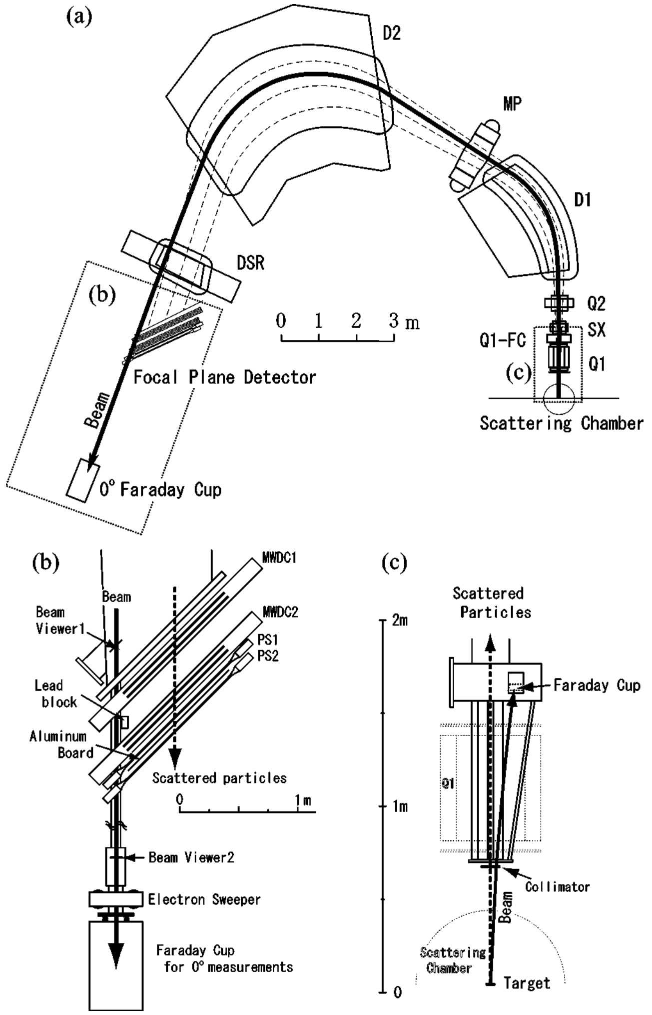

FIG. 1. Schematic layout of the experimental setup. The beam path is shown by a thick solid line. (a) The experimental setup of the 0° measurement. (b) An enlarged view of the focal-plane detector. (c) The schematic view of the experimental setup for the 2°–6° measurements.

In the second setting (for the measurements at forward angles from 2° to 6°), the beam passed through the 26-mm side gap of the first Q magnet ($Q1$) of the spectrometer, and stopped in a Faraday cup ($Q1$-FC) [16] placed 1.55 m behind the target position. Since the beam was deflected outwards by the magnetic field of the $Q1$ side gap, the background due to edge scattering from the FC decreased significantly. Figure 1(c) shows the schematic layout of the second setting. Again, the trigger rate without the target was lower than 5 cps for 1 nA.

In the measurements beyond 6°, a FC located in the scattering chamber was used. The beam correction efficiencies for all three FC's were in agreement within ±1% of each other.

Energy spectra were obtained for these targets in the energy range of $8 < E_x < 33$ MeV at several angles between 0° and 9° (for ^{144}Sm, up to 13.5°); the scattering angles were averaged over the acceptance of Grand Raiden. The momen-

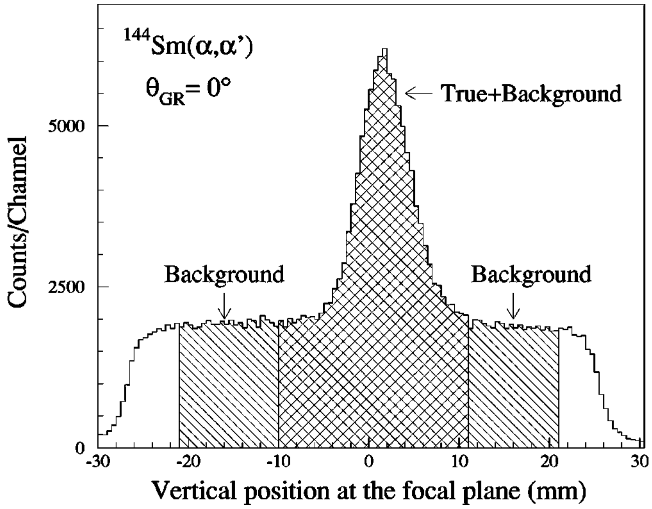

FIG. 2. Vertical-position spectrum at the focal plane of Grand Raiden taken at 0°. The central hatched region represents true + background events. The off-center regions represent only background events. The true events were extracted by subtracting the background events from the true + background events.

tum calibration was obtained from the actual magnetic-field settings of the spectrometer. The absolute beam energy was determined from the kinematic crossover angle between the elastic scattering off hydrogen and the ^{12}C inelastic scattering peaks. To check the calibration, elastic and inelastic scattering peaks of ^{12}C were measured with several magnetic-field settings for the spectrometer; the energies of the low-lying states in ^{12}C were reproduced with errors of ±30 keV.

The ion-optics of Grand Raiden enables particles scattered from the target position to be focused vertically and horizontally at the focal plane. Using this property, the instrumental background was completely eliminated. While inelastically scattered α particles are focused at the focal plane vertically, background events due to the rescattering of α particles from the wall and pole surfaces of the spectrometer show a flat distribution in the vertical position spectra at the focal plane, as shown in Fig. 2. The vertical center (cross hatched) region was treated as true + background. The off-center (slant hatched) regions were treated as background only. Figure 3(a) shows the excitation-energy spectrum for ^{144}Sm at 0° obtained from each region. The background spectrum has no distinct structure in the giant resonance region. Finally, we have obtained clean spectra by subtracting the background spectrum from the true + background spectrum, as shown in Fig. 3(b).

The energy spectra at 0° (average angle 0.7° in the laboratory frame) are shown in Fig. 4 for the Sm isotopes investigated in this work. The ratio of the peak to the continuum in the giant resonance region is about 6 in all cases. This has been possible because of practically complete elimination of all "nonphysical" backgrounds in our data. The samarium targets contained about 0.1–0.4% hydrogen contaminant; the contributions from that were subtracted using data taken with ^{12}C and polyethylene targets.

III. MULTIPOLE DECOMPOSITION ANALYSIS

In order to identify strengths corresponding to different giant resonances, we have divided inelastic scattering spectra into 1-MeV bins and carried out a multipole-decomposition (MD) analysis [17] for the angular distribution of the cross section for each bin. In this method, the experimentally obtained cross sections $\sigma^{exp}(\theta, E_x)$ are expressed as the sum of the contributions from various multipole components:

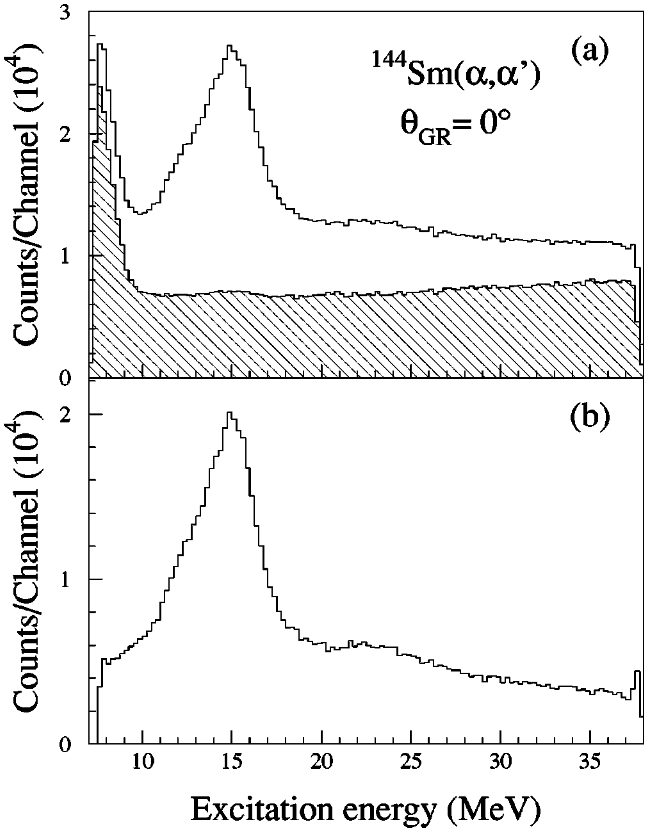

FIG. 3. (a) Excitation-energy spectrum of the ^{144}Sm(α, α') reaction at 0° for the vertical center region at the focal plane. The hatched spectrum corresponds to the off-center region (see Fig. 2). (b) Excitation-energy spectrum after background subtraction.

$$\sigma^{exp}(\theta, E_x) = \sum_L a_L(E_x)\sigma_L^{calc}(\theta, E_x), \tag{1}$$

where E_x and θ are the excitation energy and the scattering angle, respectively, and $\sigma_L^{calc}(\theta, E_x)$ is the distorted-wave Born approximation (DWBA) cross section exhausting 100% of the energy-weighted sum-rule (EWSR) value for the transferred angular momentum L. Since the experimental cross sections were obtained from the summation of the yield of the particles scattered within the acceptance of Grand Raiden, the DWBA cross sections $\sigma_L^{calc}(\theta, E_x)$ were calculated by taking a weighted average of the angular distribution over the opening angle of the spectrometer. The physical continuum underlying the giant resonances was included in the MD analysis, assuming that it can be represented as an incoherent sum of the contributions from various multipoles.

The fractions of the EWSR, $a_L(E_x)$, for various multipole components were determined by minimizing χ^2. This is quite appropriate since the angular distributions are characterized

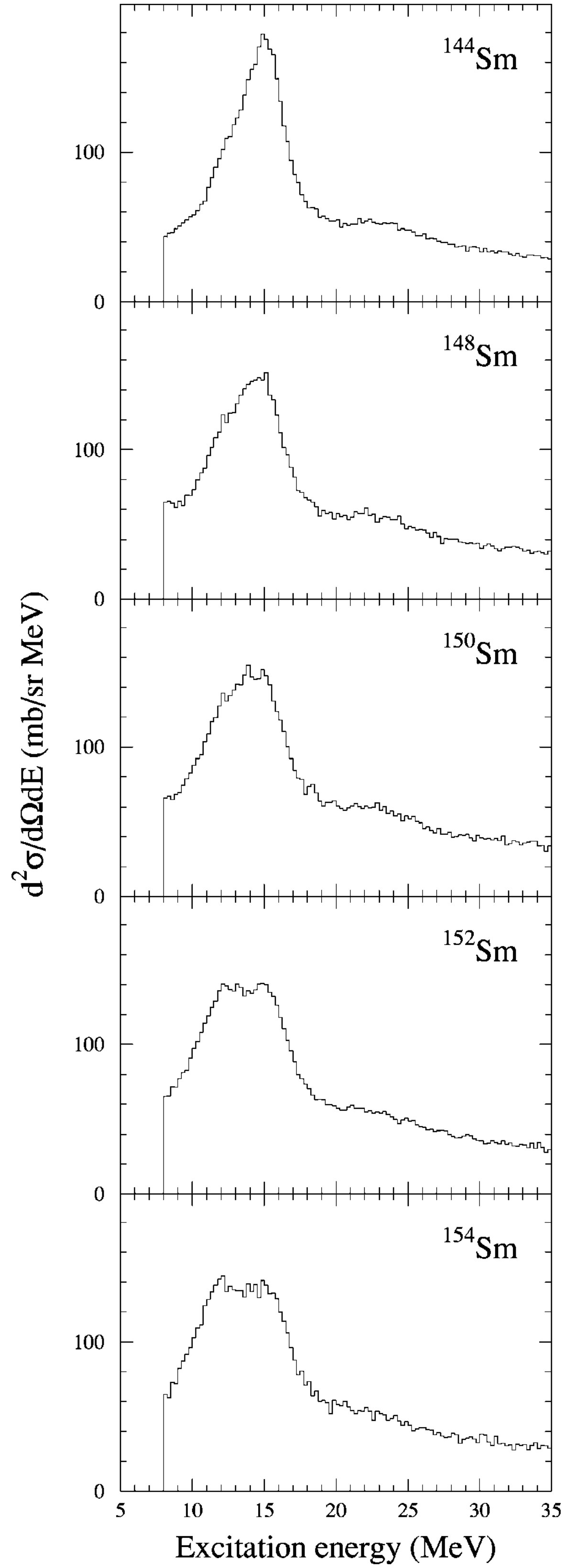

FIG. 4. Inelastic α-scattering spectra at $0°(\theta_{av}=0.7°)$ and $E_\alpha=386$ MeVfor $^{144-154}$Sm obtained in the present work. These spectra have been subtracted from the background reasonably as shown in Fig. 3.

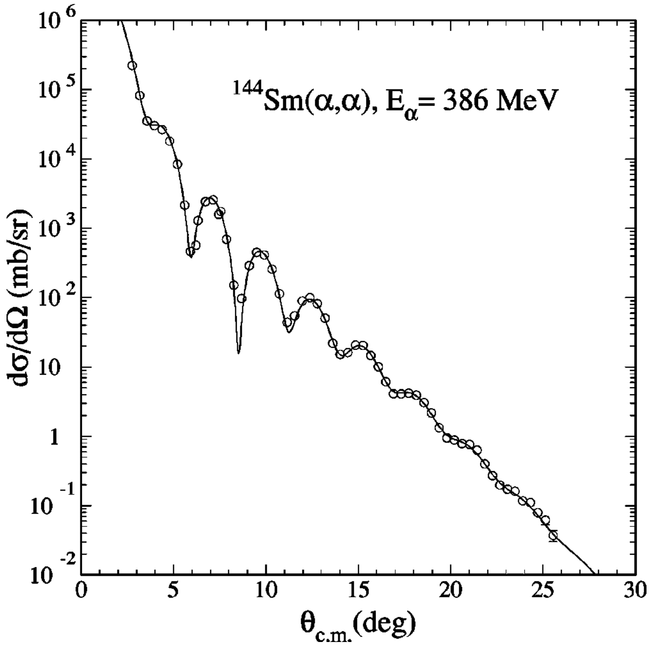

FIG. 5. Differential cross sections of elastic α-particle scattering from ^{144}Sm at 386 MeV. The open circles show the measured cross sections. The solid line shows the result of the DW calculation with an optical-model potential obtained via a single-folded potential model.

by the transferred angular momentum L, according to the DWBA calculations for α scattering.

In the DWBA calculations, a single-folded potential model was employed, with a nucleon-α interaction of the density-dependent Gaussian form, as described in Refs. [18,19]. The nucleon-α interaction is given by

$$V[|\mathbf{r}-\mathbf{r}'|,\rho_0(r')] = -V[1+\beta_V\rho_0(r')^{2/3}]\exp(-|r-r'|^2/\alpha_V) - iW[1+\beta_W\rho_0(r')^{2/3}]\exp(-|r-r'|^2/\alpha_W), \tag{2}$$

where the ground state density $\rho_0(r')$ was obtained using the relativistic mean-field (RMF) calculation code TIMORA [20]. The parameters V, W, $\alpha_{V,W}$, and $\beta_{V,W}$ in Eq. (2) were determined by fitting the differential cross sections of elastic α scattering measured for ^{144}Sm at $E_\alpha=386$ MeV; the fit is shown in Fig. 5. The nucleon-α interaction parameters are listed in Table I, and were also used in the calculation of optical-model potentials and transition densities for the other Sm isotopes.

The following collective isoscalar transition densities were used:

TABLE I. The nucleon-α interaction parameters.

	V (MeV)	α_V (fm^2)	W (MeV)	α_W (fm^2)	$\beta_{V,W}$ (fm^2)
^{144}Sm	28.20	4.1	15.79	4.2	-1.9^{a}

[a] Taken from Refs. [18,19].

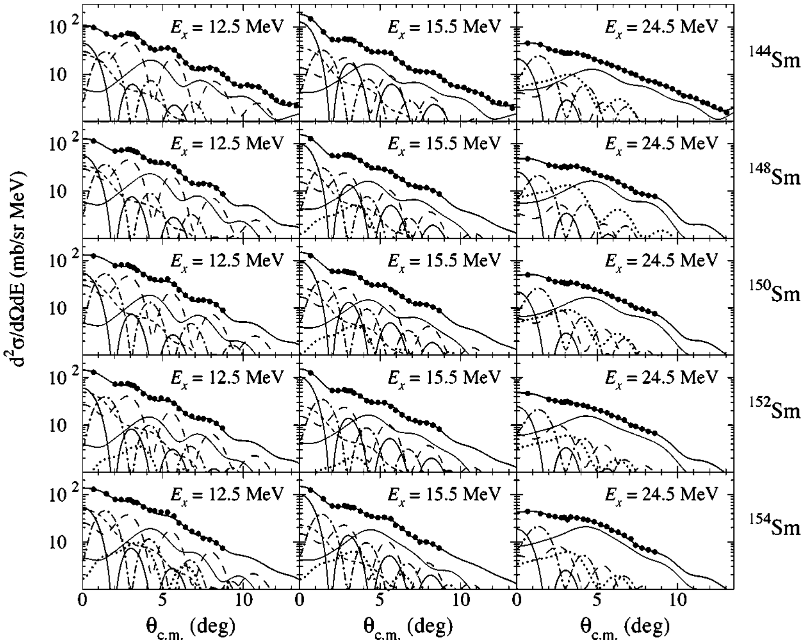

FIG. 6. Double-differential cross sections for selected energy bins in $^{144-154}$Sm. The solid lines through the data show fits to the data from multipole decomposition. In each panel, the contributions from $L=0$ (thick-solid), $L=1$ ($T=0$) (dot-dashed), $L=1$ ($T=1$) (short-dashed), $L=2$ (long-dashed), $L=3$ (dotted), and $L\geqslant 4$ (thin-solid) are also displayed.

$$\delta\rho_{L=0}(r,E_x)=-\beta_0(E_x)\left(3+r\frac{d}{dr}\right)\rho_0(r), \tag{3}$$

$$\delta\rho_{L=1}(r,E_x)=-\frac{\beta_1(E_x)}{R\sqrt{3}}\left[3r^2\frac{d}{dr}+10r-\frac{5}{3}\langle r^2\rangle\frac{d}{dr}+\epsilon\left(r\frac{d^2}{dr^2}+4\frac{d}{dr}\right)\right]\rho_0(r), \tag{4}$$

$$\delta\rho_{L\geqslant 2}(r,E_x)=-\frac{\beta_{L\geqslant 2}(E_x)R}{\sqrt{2L+1}}\left(\frac{r}{R}\right)^{L-1}\frac{d}{dr}\rho_0(r), \tag{5}$$

where $\langle r^N\rangle$ and R are, respectively, the Nth moment of the ground-state density and the half-density radius of the nuclei, and $\epsilon=(4/E_2+5/E_0)\hbar^2/3mA$ (E_0,E_2 are the centroid energies of the GMR and the GQR, respectively). These transition densities are described by Satchler [21] for the GMR ($L=0$) and $L\geqslant 2$ (Tassie transition density), and by Harakeh and Dieperink [22] for the ISGDR.

Assuming that the strength of each transition is exhausted by one state at the excitation energy of E_x, the deformation parameters $\beta_L(E_x)$, used to calculate the cross sections for the 100% EWSR fraction, are given by

$$\beta_0^2(E_x)=\frac{2\pi\hbar^2}{mA\langle r^2\rangle E_x}, \tag{6}$$

$$\beta_1^2(E_x)=\frac{6\pi\hbar^2}{mAE_x}R^2\bigg/\left(11\langle r^4\rangle-\frac{25}{3}\langle r^2\rangle^2-10\epsilon\langle r^2\rangle\right), \tag{7}$$

$$\beta_{L\geqslant 2}^2(E_x)=\frac{2\pi\hbar^2LR^{2L-4}}{mA\langle r^{2L-2}\rangle E_x}, \tag{8}$$

where m and A are the nucleon mass and the target mass number, respectively. These deformation parameters and transition densities are also given in Ref. [23].

Even in scattering of isoscalar probes, such as α particles, the isovector giant dipole resonance (IVGDR) may be excited by the Coulomb interaction and hadronic interaction due to the difference between the proton and neutron densities for $N\neq Z$ nuclei (N, Z are the numbers of neutrons and protons, respectively). The IVGDR transition density and deformation parameter were given in Ref. [21] as

$$\delta\rho_{1,T=1}(r,E_x)=\beta_{1,T=1}(E_x)\gamma\frac{N-Z}{A}\left(\frac{d}{dr}+\frac{1}{3}c\frac{d^2}{dr^2}\right)\rho_0(r), \tag{9}$$

$$\beta_{1,T=1}^2(E_x)=\frac{\pi\hbar^2}{2m}\frac{A}{NZE_x}, \tag{10}$$

where $\gamma=3(c_n-c_p)A/[2c(N-Z)]$, and c_n, c_p, c are the half radii of the neutron, proton, and nucleon distributions, respectively. The contribution from the IVGDR was estimated using the strength distribution deduced from the photoneutron cross sections [24]. Contributions from the Coulomb excitation of the higher multipolarity isovector states are negligibly small according to the theoretical calculations of Auerbach and Klein [25].

The DWBA calculations were carried out with the code ECIS95 [26] using external potentials. Multipole components up to $L_{max}=19$ for ^{144}Sm, and $L_{max}=12$ for $^{148-154}$Sm were taken into account in the fits. The reduced chi-squares (χ^2/ν) were between 1 and 5, where ν was the number of the degrees of freedom. The fitting errors were estimated by changing the magnitude of one component $a_L(E_x)$, until refitting by varying the other components resulted in an increase in the χ^2 by 1. The number of data points, 34 for ^{144}Sm, 22 for ^{154}Sm, and 21 for ^{148,150,152}Sm, were enough to obtain unique solutions in the fit. Figure 6 shows the results

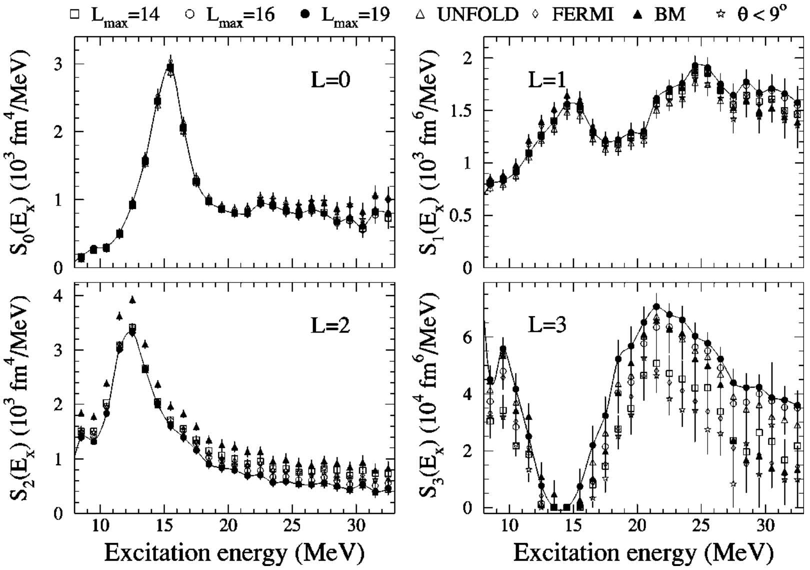

FIG. 7. The results of the MD analysis in ^{144}Sm with various choices for L_{max}, ground-state density, and transition density. The solid lines connect data points. The closed circles, open circles, and open squares, respectively, show the results for L_{max} (14, 16, and 19). The open triangles (UNFOLD) and open diamonds (FERMI) show the results of the MD analysis with the DWBA angular distributions calculated from the ground-state densities distributions in two alternative models. The closed triangles (BM) show the results with the DWBA angular distributions calculated from the Bohr-Mottelson transition density. The open stars show the results from the data of the $\theta_{\mathrm{c.m.}} < 9°$ for ^{144}Sm. See text for more details.

of multipole fits to angular distributions for several excitation-energy bins in $^{144-154}$Sm.

The strength distributions obtained from the MD analysis depend on calculated angular distributions and are affected by the choices made for, e.g., the L_{max}, the ground-state density and the transition density. Figure 7 shows the results of the MD analysis for various choices in the ^{144}Sm data, starting from the results obtained with the ground-state density obtained from RMF calculations, transition densities from Eqs. (6)–(8), and $L_{max}=19$. Here, L_{max} is the maximum number of L taken into consideration in the MD analysis in Eq. (1). UNFOLD and FERMI show the results corresponding to alternative model of the ground-state density used in the DWBA calculation. In UNFOLD, the ground-state density is calculated from the charge density and the nucleon form factor, whereas in FERMI a Fermi-type density distribution with $c=6.039$ fm and $a=0.470$ taken from Ref. [27] is used. UNFOLD has been applied in our earlier work [14]. However, since the proton and neutron density distributions are assumed to be same, the UNFOLD density is not realistic for the $N \neq Z$ nuclei. The nucleon-α interaction parameters were independently determined by fitting the elastic scattering angular distribution using each ground-state density. BM corresponds to substituting the Tassie transition densities in Eq. (5) by the transition density of a surface vibration [28], which is often used for the analysis of the giant resonances with $L \geqslant 2$ [21].

The results for the $L=0$ are practically independent of the choices mentioned above. The $L=1$ strength distributions are independent of the choice of the L_{max}'s; however, changing the ground-state densities resulted in changes in the extracted strength of up to 10% in the high-excitation-energy region. For $L=2$, the effect of changing the transition density is to change the calculated cross section for the 100% EWSR fraction, $\sigma_2^{calc}(\theta, E_x)$, by ~20%; the results are unaffected by changes in L_{max} and the ground-state density. The largest effects are observed for the high-excitation region of the $L=3$ strength distribution. To see the effect of the lack of large angle data ($\theta > 9°$) for all targets other than ^{144}Sm, we carried out the MD analysis with the use of angular distribution data less than 9° for ^{144}Sm. The effects were the same as those of various choices used when calculating the angular distributions. Similar effects are observed in the other samarium nuclei as well. The slight differences between the results reported in our earlier work [14] and the present results come mainly from these uncertainties.

IV. DISCUSSION

A. Coupling between the GMR and the GQR

The extracted GMR and GQR strength distributions for the Sm isotopes are shown in Fig. 8. Both the GMR and GQR strengths have a clear peak each, but also extend to higher excitation energies. The total EWSR fractions integrated over the measured excitation-energy regions are over 150%. However, as pointed out in the preceding section, the strength distributions obtained from comparison with the DWBA cross sections depend on the transition densities used in the analysis. Thus, a possible reason for the excess in the EWSR fractions is that the macroscopic transition densities of the GMR and GQR used in this analysis are not valid in the high-excitation-energy region. Therefore, further analyses were carried out for the energy regions, from 9 to 18 MeV for the GMR, and from 9 to 16 MeV for the GQR. In the spherical nucleus ^{144}Sm, the GMR and the GQR were each fitted with a Breit-Wigner function. The fitting parameters are listed in Table II; the EWSR fractions for individual peaks are obtained by integrating the Breit-Wigner functions from 8 to 33 MeV; the "total" EWSR fraction listed is the experimental strength integrated over the energy region. Even if the shape of the high-excitation-energy tail is described by a polynomial function beginning with the particle threshold energy (~8 MeV), fitting parameters (peak positions, widths, and EWSR fractions) in Table II are not changed so much. These changes in the fittings parameters are included in the errors. Naturally, the introduction of the polynomial function to describe the continuum tends to reduce the EWSR fractions of the high-excitation-energy (HE) component. The errors arising from the differences of the fitting regions were not included.

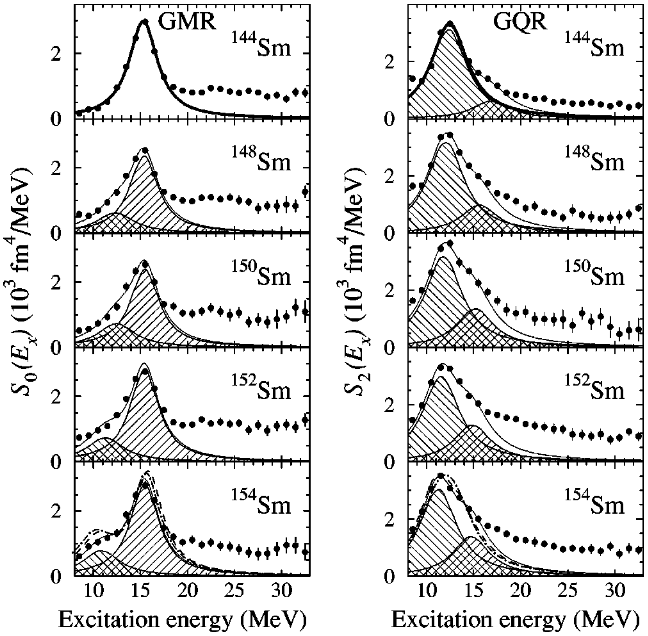

FIG. 8. The $L=0$ and $L=2$ strength distributions for $^{144-154}$Sm obtained from the multipole-decomposition analysis (see text). The thick solid lines show the results of a Breit-Wigner fit. The thin solid lines show the results of two-Breit-Wigner fits to the peak region. The low- and high-excitation-energy components of the GMR and the GQR are indicated by slashed areas. For the result of ^{154}Sm, the calculations of the adiabatic cranking model (dashed lines) [7] and the fluid-dynamical model (dash-dotted lines) [11] are shown.

The GMR strength is expected to split into two components because of the coupling to the GQR. For comparison with the theoretical results, the "peak region" of the GMR in $^{148-154}$Sm was fitted with two-Breit-Wigner functions. The widths were fixed using those of the GQR and the GMR in ^{144}Sm, since the "lower" component of the GMR arises from the mixing with the $K=0$ component of the GQR. The GQR strength, on the other hand, is predicted to split into three components by Abgrall *et al.* [7] and four components by Nishizaki and Andō [11]. However, the strength distributions for the GQR were fitted with only two-Breit-Wigner functions in the excitation-energy region from 9 to 16 MeV, because very small strengths are associated with the other components in the theoretical predictions. The results of the two-Breit-Wigner fit for $^{144-154}$Sm are also presented in Table II. It should be noted that even though the peak positions were treated as free parameters in these fits, the low-energy components of both the GMR and GQR appear at more-or-less the same energy, as expected from their mixing. We notice that the HE component of the GQR caused by the K splittings seems to increase with increasing nuclear deformation, though a small HE component exists in ^{144}Sm.

Figure 9 compares the peak energy of each component with that from the two theoretical models, viz., the adiabatic cranking model of Abgrall *et al.* [7] and the fluid-dynamical model of Nishizaki and Andō [11]. Both models reproduce well the peak energies of the HE component of the GMR. However, the experimental low-excitation-energy (LE) components are higher in energy than the theoretically predicted values. A similar behavior has been observed for ^{154}Sm by Youngblood *et al.* [6].

Figure 8 also shows a comparison between the fits with two-Breit-Wigner functions to the GMR and GQR peaks in ^{154}Sm and the strength distributions obtained from two theoretical models. The theoretical GMR strength was also calculated with two-Breit-Wigner functions. The width of the LE component, which couples with the $K=0$ component of

TABLE II. The parameters for fits to the strength distributions of the GMR and GQR. The peak energy, width, and the EWSR fractions obtained in the Breit-Wigner fits are listed.

		LE component			HE component			Total
Target	Fit-region (MeV)	Peak (MeV)	Width (MeV)	EWSR (%)	Peak (MeV)	Width (MeV)	EWSR (%)	EWSR (%)
GMR								
^{144}Sm^{a}	9–18				$15.30^{+0.11}_{-0.12}$	$3.71^{+0.12}_{-0.63}$	84^{+4}_{-25}	169±4
^{148}Sm	9–18	12.32±0.45	4.7^{b}	17^{+3}_{-4}	$15.37^{+0.14}_{-0.18}$	3.7^{c}	64^{+5}_{-24}	185±5
^{150}Sm	8–18	$12.5^{+1.7}_{-1.5}$	4.7^{b}	19±11	15.48±0.28	3.7^{c}	63^{+13}_{-28}	188±7
^{152}Sm	9–18	$11.27^{+0.32}_{-0.54}$	4.7^{b}	17^{+2}_{-4}	$15.44^{+0.12}_{-0.23}$	3.7^{c}	73^{+4}_{-25}	206±5
^{154}Sm	9–18	$10.83^{+0.32}_{-0.54}$	4.7^{b}	17^{+2}_{-3}	$15.45^{+0.13}_{-0.16}$	3.7^{c}	71^{+4}_{-23}	172±6
GQR								
^{144}Sm^{a}	9–15	12.43±0.11	4.72±0.17	95^{+4}_{-7}				165±4
^{144}Sm	9–16	12.33±0.11	4.7^{b}	88±4	16.9±1.3	4.7^{b}	24^{+14}_{-17}	
^{148}Sm	9–16	12.03±0.13	4.7^{b}	84±5	$15.61^{+0.85}_{-0.68}$	4.7^{b}	34^{+5}_{-6}	188±6
^{150}Sm	9–16	11.81±0.17	4.7^{b}	80±6	15.15±0.51	4.7^{b}	44^{+7}_{-14}	214±9
^{152}Sm	9–16	11.53±0.14	4.7^{b}	71±5	14.86±0.39	4.7^{b}	40^{+5}_{-17}	222±5
^{154}Sm	9–16	11.24±0.14	4.7^{b}	69±4	$14.73^{+0.35}_{-0.32}$	4.7^{b}	42^{+5}_{-14}	215±5

[a] The result of a single-Breit-Wigner fit.
[b] The width of the GQR in ^{144}Sm.
[c] The width of the GMR in ^{144}Sm.

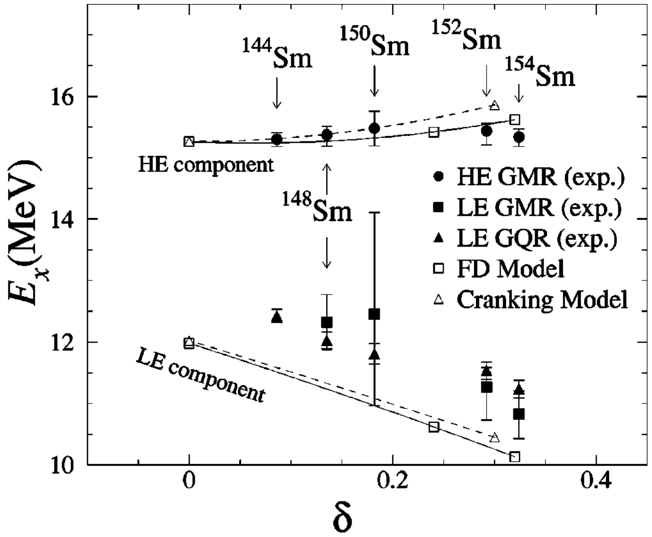

FIG. 9. The peak energies for the GMR and for the K=0 components of the GQR in $^{144-154}$Sm are plotted as a function of the deformation parameter δ. The open squares are results of the fluid-dynamical model. The open triangles are results of the cranking model. The lines are drawn to guide the eye.

the GQR, was taken to be equal to that of the GQR, and that of the HE component as equal to that of the GMR in ^{144}Sm. For the calculated GQR strength distributions, the predicted number of Breit-Wigner functions was employed with the width of each taken as equal to that of the GQR in ^{144}Sm. In addition, the theoretical strength distributions were shifted to a higher excitation energy by about 0.6 MeV. As shown in Fig. 8, both theoretical GMR and GQR strength distributions are in good agreement with the experimental strengths, except for the aforementioned shift in the GQR energy.

B. The isoscalar giant dipole resonance

The extracted ISGDR strength distributions are shown in Fig. 10. Although the ISGDR strength was calculated only for one of the magnetic substates in our earlier paper [14], we have taken into account all the substates, resulting that the present ISGDR strength are larger by a factor of 3 than the previous results. Since the ISGDR strength distribution has been known to consist of two components [14,29,30], the strength in ^{144}Sm was fitted with two-Breit-Wigner functions. The HE component at E_x=$25.0^{+1.7}_{-0.3}$ MeV contained 91^{+25}_{-17}% of the E1 EWSR value, and the LE component at E_x=14.2±0.2 MeV contained 23^{+4}_{-10}% of the E1 EWSR value. The error reflects the effect of the choice for the range for the Breit-Wigner fits (12–28 MeV and 12–33 MeV).

The observed ISGDR distribution was roughly divided into an LE component (8–17 MeV) and an HE component (17–33 MeV) as indicated by a dashed line in Fig. 10. The centroid energy and the EWSR fraction of each component are listed in Table III. The centroid energy was calculated by the following equations:

$$E^C = \frac{m_1}{m_0}, \tag{11}$$

where m_k is the kth moment of the strength distribution, m_k=$\int E_x S(E_x) dE_x$. Except for ^{150}Sm, the EWSR fraction of the LE component increased smoothly with nuclear deformation, whereas that of the HE component did not change. The ratio of the EWSR fraction of the LE component to that of the HE component increases monotonically as the nuclear deformation for the measured samarium isotopes.

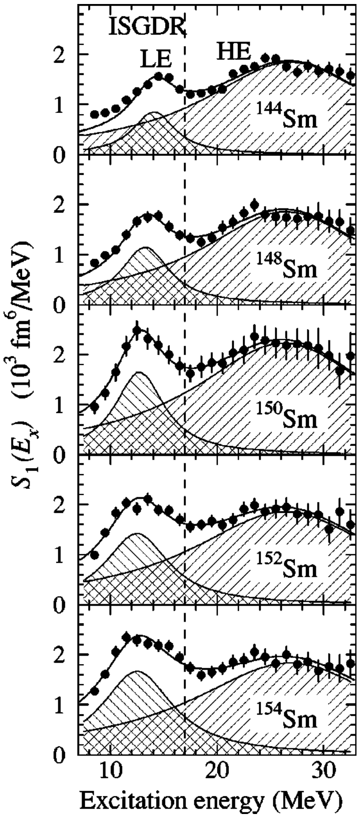

FIG. 10. The ISGDR strength observed in the Sm isotopes. The dashed line indicates the division between the LE and HE components (see text). The results of two-Breit-Wigner fits are also shown.

The widths (Γ) obtained by the two-Breit-Wigner fit are also listed in Table III. The widths of the LE component were broadened with increasing nuclear deformation.

C. The high-energy octupole resonance

Figure 11 shows the extracted L=3 strength distributions. There are two components in the L=3 resonance: the low-energy, $1\hbar\omega$, 3^- resonance (LEOR), and the high-energy, $3\hbar\omega$, 3^- resonance (HEOR). In previous measurements [13,31,32], the LEOR and HEOR strengths have been found at about $30A^{-1/3}$ and $110A^{-1/3}$ MeV. In ^{144}Sm, these correspond to 6 and 21 MeV, respectively. In this section, only the HEOR region (over 10 MeV) is discussed; the LEOR lies below the lower-excitation-energy bound of our measurement.

The HEOR region was also divided into two parts as the ISGDR: The LE part encompassing the excitation-energy range 10–17 MeV and the HE part17–33 MeV. The centroid energy and the EWSR fractions for each part are listed in Table. IV. The HEOR strength appears to shift towards lower excitation energy with increasing nuclear deformation, since the ratio of the EWSR fraction of the LE part to that of the

TABLE III. The centroid energy and width for each component of the ISGDR.

Target	LE component			HE component			
	E^C (MeV)	Γ (MeV)	EWSR (%)	E^C (MeV)	Γ (MeV)	EWSR (%)	$\frac{\text{EWSR(LE)}}{\text{EWSR(HE)}}$
^{144}Sm	13.04±0.34	4.8±0.8	23±1	25.4±0.6	19.9±1.9	109±2	0.21
^{148}Sm	12.95±0.45	5.6±0.9	25±1	25.2±1.1	19.4±2.8	103±3	0.24
^{150}Sm	12.91±0.61	5.6±1.3	33±2	25.1±1.4	20.7±4.5	122±5	0.27
^{152}Sm	12.77±0.37	7.2±0.9	29±1	25.1±1.0	21.6±3.4	103±3	0.29
^{154}Sm	12.75±0.33	8.2±1.0	32±1	25.1±1.0	22.6±4.2	102±3	0.32

HE part increases with increasing nuclear deformation. Such a shift for the HEOR in deformed nuclei was also reported by Morsch *et al.* [13].

D. Coupling between the ISGDR and the HEOR

The isoscalar odd-parity giant resonances, the ISGDR and the HEOR, are also expected to couple [11]. As seen in Tables III and IV, the ratios of the LE part and the HE part for both the ISGDR and HEOR increase monotonically with increasing deformation. This implies a shift of strength from the HE part to the LE part that is consistent with a mixing between the $K=0$ and $K=1$ components of the two resonances. The data, thus, provide evidence for the expected mixing.

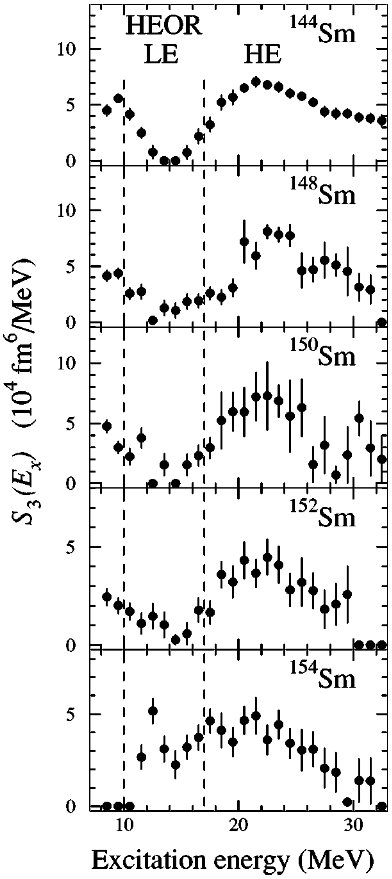

FIG. 11. The $L=3$ strength observed in the Sm isotopes. The dashed lines indicate the regions of the LE and HE parts, respectively (see text).

However, as pointed out in Ref. [14], a direct comparison of the observed ISGDR strength in ^{154}Sm with theoretical predictions is complicated by the nature of the LE component of the ISGDR in spherical nuclei. According to recent theoretical work on the ISGDR [33–37], this LE component is of "nonbulk" origin—only the HE component of the ISGDR strength corresponds to a compressional mode. On the other hand, considering the effects of deformation on the ISGDR and HEOR, Ref. [11] takes into account only the coupling between the HEOR and the compressional-mode ISGDR. Further theoretical work to investigate the effect of deformation on the "nonbulk" LE component of the ISGDR strength is clearly most urgently warranted.

V. SUMMARY

Double-differential cross sections of inelastic α scattering at $E_\alpha=386$ MeV were measured for the ^{144,148,150,152,154}Sm targets practically without any instrumental background. Measured angular ranges were $0°\leqslant\theta_{lab}\leqslant 9°$ ($13°$ for ^{144}Sm). Measured excitation-energy ranges were $8\leqslant E_x\leqslant 33$ MeV. Energy spectra were analyzed by the multipole decomposition technique, using DWBA angular distributions calculated in the framework of the single-folding model with a density-dependent nucleon-α interaction. The strength distributions for the GMR, ISGDR, GQR, and HEOR were determined for the measured nuclei.

We have observed splitting of the GMR strength due to the mixing between the GMR and GQR in deformed nuclei.

TABLE IV. The centroid energy for each part of the HEOR.

Target	LE part		HE part		
	E^C (MeV)	EWSR (%)	E^C (MeV)	EWSR (%)	$\frac{\text{EWSR(LE)}}{\text{EWSR(HE)}}$
^{144}Sm	12.5±2.5	5±1	24.5±0.8	76±2	0.06
^{148}Sm	13.2±2.9	5±1	24.4±2.6	65±5	0.08
^{150}Sm	13.1±3.5	5±1	23.9±4.2	58±8	0.09
^{152}Sm	13.2±3.8	3±1	123.1±3.6	31±4	0.11
^{154}Sm	14.0±1.7	9±1	22.8±2.9	34±3	0.27

The peak energies of the high-excitation-energy component of GMR are in good agreement with the predictions of the adiabatic cranking model of Abgrall *et al.* [7] and the fluid-dynamical model of Nishizaki and Andō [11]. However, the low-excitation-energy components, which correspond to the coupling between the GMR and GQR, are ~0.6 MeV higher than those predicted by the theory. The strength distributions of the GMR and GQR in ^{154}Sm are in good agreement with the calculations, if the GQR is artificially shifted to a higher excitation energy by ~0.6 MeV. For the ISGDR, the effects of the deformation were different for the low- and high-excitation-energy components: The width and strength of the low-excitation-energy component increase with increasing nuclear deformation, whereas the high-excitation-energy component hardly changes. The expected coupling [11] between odd-parity giant resonances, the ISGDR and the HEOR, was evidenced for the first time via an enhancement and broadening of the low-excitation-energy component of the ISGDR, and for the shift of the HEOR strength towards lower excitation energies.

ACKNOWLEDGMENTS

We gratefully thank Professor K. Hatanaka and the RCNP cyclotron staff for their efforts in preparing halo-free beams and thank P. Boutachkov for his help with the initial experimental run. This work was supported in part by the U.S.-Japan Cooperative Science Program of the JSPS and the U.S. National Science Foundation (Grant Nos. INT-9910015, PHY-9901133, and PHY-010324), and the University of Notre Dame.

---

[1] U. Garg, P. Bogucki, J. D. Bronson, Y.-W. Lui, C. M. Rozsa, and D. H. Youngblood, Phys. Rev. Lett. **45**, 1670 (1980).
[2] T. Kishimoto, J. M. Moss, D. H. Youngblood, J. D. Bronson, C. M. Rozsa, D. R. Brown, and A. D. Bacher, Phys. Rev. Lett. **35**, 552 (1975).
[3] H. Miura and Y. Torizuka, Phys. Rev. C **16**, 1688 (1977).
[4] M. Buenerd, D. Lebrun, Ph. Martin, P. de Saintignon, and C. Perrin, Phys. Rev. Lett. **45**, 1667 (1980).
[5] R. De Leo, S. Brandenburg, A. G. Drentje, M. N. Harakeh, H. Janszen, and A. van der Woude, Nucl. Phys. **A441**, 591 (1985).
[6] D. H. Youngblood, Y.-W. Lui, and H. L. Clark, Phys. Rev. C **60**, 067302 (1999).
[7] Y. Abgrall, B. Morand, E. Caurier, and B. Grammaticos, Nucl. Phys. **A346**, 431 (1980).
[8] T. Suzuki and D. J. Rowe, Nucl. Phys. **A289**, 461 (1977).
[9] N. Auerbach and A. Yeverechyahu, Phys. Lett. **62B**, 143 (1976).
[10] D. Zawischa, J. Speth, and D. Pal, Nucl. Phys. **A311**, 445 (1978).
[11] S. Nishizaki and K. Andō, Prog. Theor. Phys. **73**, 889 (1985).
[12] D. H. Youngblood, H. L. Clark, and Y.-W. Lui, RIKEN Rev. **23**, 159 (1999).
[13] H. P. Morsch *et al.*, Phys. Lett. **119B**, 311 (1982).
[14] M. Itoh *et al.*, Phys. Lett. B **549**, 58 (2002).
[15] M. Fujiwara *et al.*, Nucl. Instrum. Methods Phys. Res. A **422**, 484 (1999).
[16] M. Itoh *et al.*, RCNP Annual Report, 1999, p. 7.
[17] B. Bonin *et al.*, Nucl. Phys. **A430**, 349 (1984).
[18] A. Kolomiets, O. Pochivalov, and S. Shlomo, Phys. Rev. C **61**, 034312 (2000).
[19] G. R. Satchler and D. T. Khoa, Phys. Rev. C **55**, 285 (1997).
[20] C. J. Horowitz, D. P. Murdock, and B. D. Serot, *Computational Nulear Physics 1* (Springer-Verlag, Berlin, 1991), Chap. 7.
[21] G. R. Satchler, Nucl. Phys. **A472**, 215 (1987).
[22] M. N. Harakeh and A. E. L. Dieperink, Phys. Rev. C **23**, 2329 (1981).
[23] M. Harakeh and A. van der Woude, *Giant Resonances* (Clarendon, Oxford, 2001).
[24] S. S. Dietrich and B. L. Berman, At. Data Nucl. Data Tables **38**, 199 (1988).
[25] N. Auerbach and A. Klein, Nucl. Phys. **A395**, 77 (1983).
[26] J. Raynal, computer code ECIS95, NEA0850-14 (1995).
[27] H. Sakaguchi, *Memoirs of the Faculty of Science, Kyoto University*, Series of Physics, Astrophysics, Geophysics and Chemistry Vol. 36 (1983), p. 306.
[28] A. Bohr and B. Mottelson, *Nuclear Structure* (Benjamin, New York, 1975), Vol. 2.
[29] H. L. Clark, Y.-W. Lui, and D. H. Youngblood, Phys. Rev. C **63**, 031301(R) (2001).
[30] M. Uchida *et al.*, Phys. Lett. B **557**, 12 (2003).
[31] J. M. Moss, D. R. Brown, D. H. Youngblood, C. M. Rozsa, and J. D. Bronson, Phys. Rev. C **18**, 741 (1978).
[32] H. L. Clark, D. H. Youngblood, and Y.-W. Lui, Phys. Rev. C **54**, 72 (1996).
[33] I. Hamamoto, H. Sagawa, and X. Z. Zhang, Phys. Rev. C **57**, R1064 (1998).
[34] G. Colo, N. Van Giai, P. F. Bortignon, and M. R. Quaglia, Phys. Lett. B **485**, 362 (2000).
[35] J. Piekarewicz, Phys. Rev. C **62**, 051304(R) (2000).
[36] D. Vretenar, A. Wandelt, and P. Ring, Phys. Lett. B **487**, 334 (2000).
[37] S. Shlomo and A. I. Sanzhur, Phys. Rev. C **65** 044310 (2002).